Journal of the Mechanics and Physics of Solids 57 (2009) 891–908

Contents lists available at ScienceDirect

Journal of the Mechanics and Physics of Solids

journal homepage: www.elsevier.com/locate/jmps

# A unified potential-based cohesive model of mixed-mode fracture

Kyoungsoo Park, Glaucio H. Paulino *, Jeffery R. Roesler

*Department of Civil and Environmental Engineering, University of Illinois at Urbana-Champaign, 205 North Mathews Ave., Urbana, IL 61801, USA*

ARTICLE INFO

*Article history:*
Received 8 August 2007
Accepted 3 October 2008

*Keywords:*
Fracture
Constitutive behavior
Energy release rate
Fracture mechanism
Cohesive fracture

ABSTRACT

A generalized potential-based constitutive model for mixed-mode cohesive fracture is presented in conjunction with physical parameters such as fracture energy, cohesive strength and shape of cohesive interactions. It characterizes different fracture energies in each fracture mode, and can be applied to various material failure behavior (e.g. quasi-brittle). The unified potential leads to both intrinsic (with initial slope indicators to control elastic behavior) and extrinsic cohesive zone models. Path dependence of work-of-separation is investigated with respect to proportional and non-proportional paths—this investigation demonstrates consistency of the cohesive constitutive model. The potential-based model is verified by simulating a mixed-mode bending test. The actual potential is named PPR (Park–Paulino–Roesler), after the first initials of the authors' last names.



## 1. Introduction

A potential function is associated with physical field quantities as a function of position at the continuum or atomistic level (e.g. gravity, strain energy, magnetic energy, electric energy). In a continuum setting, strain-energy functions allow the determination of stresses and the stiffness distributions in a solid. For isotropic and incompressible materials, the general strain-energy function can be deduced from the linear relationship between shear and traction (Mooney, 1940). At the atomistic level, pair potentials are mostly utilized to represent the particle debonding process as a function of an atomic distance ($\ell$) such as the Lennard–Jones potential. The general shape of atomistic potentials (Girifalco and Weizer, 1959) is shown in Fig. 1(a). A potential function must have a minimum at some point because the interaction force, i.e. the derivative of the potential, must be attractive at large distances, and repulsive at smaller distances. The work to complete dissociation ($\Psi_0$) of an interaction should be finite, which corresponds to the area under the interaction force curve (Fig. 1(b)). When the distance between particles becomes critical ($\ell_{cr}$), the interaction reaches a bifurcation point. The potential ($\Psi$) has a convex shape ($\Psi''>0$) before the bifurcation, and a concave shape ($\Psi''<0$) after the bifurcation point.

For the analysis of deformation and failure mechanisms, an atomistic potential is connected to a macroscopic continuum potential through multi-scaling techniques. Tadmor et al. (1996) proposed the quasi-continuum method for the analysis of coupled atomistic/continuum deformation process in crystals based on an atomistic energy function. Gao and Klein (1998) developed the virtual internal bond model, which connects the interatomic bonding to the continuum cohesive failure through the Cauchy–Born rule. The model combines elastic and fracture behavior within the framework of continuum mechanics. The virtual internal bond model has been successfully utilized to describe crack nucleation and growth for various materials (Klein and Gao, 1998; Gao and Ji, 2003; Thiagarajan et al., 2004; Park et al., 2008b). Moreover, it has been modified by Volokh and Gao (2005) to account for two independent linear elastic constants.

* Corresponding author. Tel.: +1 217 333 3817; fax: +1 217 265 8641.
*E-mail address:* paulino@uiuc.edu (G.H. Paulino).

0022-5096/$ - see front matter © 2009 Elsevier Ltd. All rights reserved.
doi:10.1016/j.jmps.2008.10.003

**Nomenclature**

*The following symbols are used in this paper:*

| | |
|---|---|
| $\langle\cdot\rangle$ | Macaulay bracket |
| $\ell$ | atomic distance |
| $\ell_{cr}$ | atomic distance at the bifurcation (critical) point |
| $m$, $n$ | non-dimensional exponents in the PPR model |
| $P$ | applied load |
| $P_{I}$, $P_{II}$ | loading parameters in mixed-mode bending tests |
| $r$ | non-dimensional parameter in the potential by Xu and Needleman (1993) |
| $T_n$, $T_t$ | normal and tangential cohesive interactions |
| $W_{sep}$ | work-of-separation |
| $W_n$, $W_t$ | work done by the normal and tangential cohesive traction |
| $\alpha$, $\beta$ | shape parameters in the PPR model |
| $\Gamma_n$, $\Gamma_t$ | energy constants in the PPR model |
| $\Delta$ | deflection in the mixed-mode bending tests |
| $\Delta_n$, $\Delta_t$ | normal and tangential separations along fractured surface |
| $\Delta_{n,max}$, $\Delta_{t,max}$ | maximum normal and tangential separations |
| $\Delta_r$ | separation for proportional path |
| $\delta_n$, $\delta_t$ | characteristic length scale parameters |
| $\bar{\delta}_n$, $\bar{\delta}_t$ | normal and tangential conjugate final crack opening widths |
| $\theta$ | separation angle |
| $\lambda$ | effective displacement |
| $\lambda_n$, $\lambda_t$ | initial slope indicators |
| $\sigma_{max}$, $\tau_{max}$ | normal and tangential cohesive strengths |
| $\phi_n$, $\phi_t$ | modes I and II fracture energies |
| $\Psi$ | potential function for cohesive fracture |

Alternatively, based on the concept of cohesive zone (Barenblatt, 1959; Dugdale, 1960), Xu and Needleman (1994) introduced the cohesive surface network to simulate crack growth and branching phenomena. Elastic deformation is represented by general volumetric elements, while cohesive fracture behavior is described by interfacial cohesive surface elements. The constitutive relationship of cohesive fracture is derived by a potential, which represents the fracture energy distribution in conjunction with separation of fractured surfaces. Due to the physical nature of a potential, the first derivative of the fracture energy potential ($\Psi$) provides the traction (cohesive interactions) over fractured surfaces, and its second derivative provides the constitutive relationship (material tangential modulus). A single potential function, therefore, characterizes the physical fracture behavior. The cohesive zone model concept has also been applied to the extended and generalized finite element methods (X-FEM and GFEM) (Wells and Sluys, 2001; Moes and Belytschko, 2002; Remmers et al., 2008).

In the cohesive zone model, the fundamental issue for simulation of failure mechanisms is the characterization of cohesive interactions between fractured surfaces. Cohesive interactions can be classified by either non-potential-based models (e.g. Yang and Thouless, 2001; Zhang and Paulino, 2005; van den Bosch et al., 2006) or potential-based models (e.g. Needleman, 1987; Beltz and Rice, 1991; Tvergaard and Hutchinson, 1993; Xu and Needleman, 1993). Non-potential-based models are relatively simple to develop cohesive interactions because a symmetric system is not required. For instance, Yang and Thouless (2001) utilized trapezoidal shaped traction–separation relationships to simulate mixed-mode fracture of plastically deforming adhesive joints. Zhang and Paulino (2005) utilized traction-based bilinear cohesive zone model for the analysis of homogeneous and functionally graded materials (FGMs) undergoing dynamic failure. Shim et al. (2006) extended the traction-based model to the displacement-based bilinear cohesive zone model in order to investigate $J$ resistant behavior of TiB/Ti FGM in conjunction with the domain integral. In addition, van den Bosch et al. (2006) proposed an alternative exponential cohesive relationship, and assessed the work-of-separation under mixed-mode condition. The main limitation of a non-potential-based model is that one does not account for all possible separation or

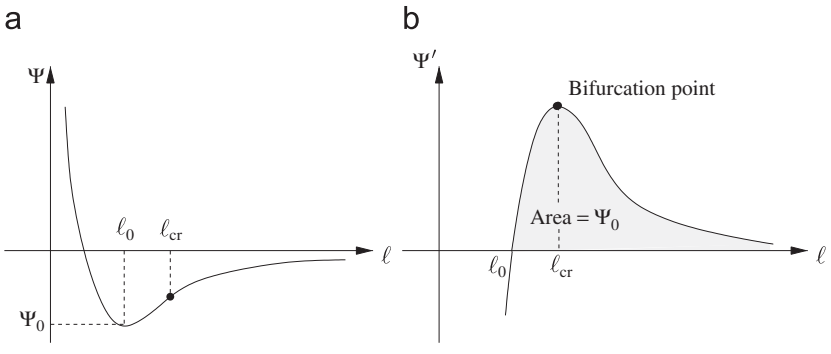


**Fig. 1.** (a) Shape of a general atomistic potential ($\Psi$) and (b) its derivative ($\Psi'$).

**Table 1**
Potentials for cohesive fracture

| Potential model | Normal interaction | Tangential interaction |
|---|---|---|
| Needleman (1987) | Polynomial | Linear |
| Needleman (1990) | Exponential | Periodic |
| Beltz and Rice (1991) | Exponential | Periodic |
| Xu and Needleman (1993) | Exponential | Exponential |
| Present (PPR model) | Polynomial | Polynomial |

loading paths of crack growth in a domain. Therefore, non-potential-based models may provide non-physical cohesive interactions, e.g. positive stiffness in a softening region, under certain mixed-mode fracture conditions, although they can capture physical fracture behavior for known crack path problems (e.g. mode I fracture or inter-layer delamination). Moreover, the tangential stiffness leads to the unsymmetric condition, which increases computational cost when solving the underlying linear system of governing equations.

For potential-based models, the one-dimensional traction potential proposed by Tvergaard and Hutchinson (1993),

$$\Psi = \delta_n \int_0^{\lambda} \sigma(\lambda')\, d\lambda', \tag{1}$$

is widely utilized to simulate interfacial fracture. The mode-mixity is considered by an effective displacement ($\lambda$) expressed as

$$\lambda = \sqrt{(\Delta_n/\delta_n)^2 + (\Delta_t/\delta_t)^2}, \tag{2}$$

where $\Delta_n$ and $\Delta_t$ are normal and tangential separations over the fractured surface, respectively, and $\delta_n$ and $\delta_t$ are characteristic length scales which are related to the fracture energy and the cohesive strength. The function $\sigma(\lambda)$ represents a traction–separation relationship. Tvergaard and Hutchinson (1992) utilized a trapezoidal shape to describe plastic behavior of ductile materials. On the other hand, Camacho and Ortiz (1996) introduced the initially rigid linear cohesive relation for adaptive insertion of cohesive surface elements, i.e. the extrinsic cohesive zone model. Ortiz and Pandolfi (1999) extended the linear cohesive relationship to the finite-deformation irreversible cohesive interaction in three dimensions. Based on linear cohesive interactions, Zhou et al. (2005) investigated fragmentation process in conjunction with strain rate and initial defects distribution, and Zhang et al. (2007) successfully simulated microbranching instability experiments.

Although the one-dimensional potential models capture fracture behavior by changing the shape of the softening curve, the models cannot have different fracture energies in modes I and II (Tvergaard and Hutchinson, 1993). However, most materials have different fracture energies with respect to the loading mode (Anderson, 1995). Several researchers have demonstrated the variation of the fracture energy from mode I fracture to mode II fracture through mixed-mode fracture specimen (Banks-Sills and Bortman, 1986) and delamination testing (Reeder and Crews, 1990; Benzeggagh and Kenane, 1996). Due to the relatively high fracture energy in mode II, a structure may have higher loading capacity under certain loading conditions. Carpinteri et al. (1989) demonstrated that mixed-mode fracture energy increased by about 30% over the mode I fracture energy for concrete. A potential function which captures the different fracture energies, therefore, is necessary for the simulation of the mixed-mode fracture.

There are several potential functions, which describe different fracture modes for cohesive fracture, as summarized in Table 1 (including the proposed one). Needleman (1987) proposed a polynomial function-based potential to simulate void nucleation by debonding. In order to account for large shear displacements, Needleman (1990) developed the exponential–periodic potential. Later, the exponential–periodic potential was generalized by Beltz and Rice (1991). The normal interaction is described by the exponential expression based on the atomistic potential by Rose et al. (1981), while the tangential interaction employs a periodic function due to the periodic dependence of the underlying material lattice (Rice, 1992). In order to consider shear failure relation, Xu and Needleman (1993) proposed the exponential potential for both normal and tangential cohesive interactions. However, the above potentials have several limitations, especially, when the mode I fracture energy is different from the mode II fracture energy (Paulino et al., 2007; Park et al., 2008a; Paulino et al., 2008).

In this study, a unified potential-based constitutive model, called PPR (Park–Paulino–Roesler), for mixed-mode cohesive fracture is developed. It characterizes different fracture energies, considers the different cohesive strengths, and describes various material softening behaviors in order to represent a wide range of failure responses. This paper is organized as follows. The unified potential-based model (PPR) for mixed-mode cohesive fracture is developed in Section 2. Section 3 discusses path dependence of the work-of-separation in the unified potential-based model for mixed-mode fracture. Section 4 verifies the proposed model. Finally, Section 5 concludes the present work.

## 2. PPR: unified potential-based constitutive model

In this section, the polynomial-based potential is proposed in conjunction with symmetric fracture boundary conditions and macroscopic fracture parameters. The proposed potential is defined in the cohesive interaction (softening) region where fractured surfaces transfer cohesive tractions. Both intrinsic and extrinsic cohesive zone constitutive models are derived from the unified potential.

### 2.1. Definition of the unified potential for mixed-mode fracture

The unified PPR potential for cohesive fracture is proposed to describe physical macroscopic fracture, including explicit control of elastic behavior for intrinsic models. Physical macroscopic behavior is represented by the following fracture boundary conditions (Fig. 2):

- Complete normal failure occurs ($T_n = 0$) when the normal or tangential separation reaches a certain length scale ($\delta_n$, $\bar{\delta}_t$), called the normal final crack opening width and the tangential conjugate final crack opening width, respectively,

$$T_n(\delta_n, \Delta_t) = 0, \quad T_n(\Delta_n, \bar{\delta}_t) = 0. \tag{3}$$

- Similarly, complete tangential failure occurs ($T_t = 0$) either when the normal separation reaches the normal conjugate final crack opening width ($\bar{\delta}_n$) or when the tangential separation reaches the tangential final crack opening width ($\delta_t$),

$$T_t(\bar{\delta}_n, \Delta_t) = 0, \quad T_t(\Delta_n, \delta_t) = 0. \tag{4}$$

- The area under the cohesive interactions corresponds to the fracture energy. Therefore ($\phi_n$, $\phi_t$) are given by

$$\phi_n = \int_0^{\delta_n} T_n(\Delta_n, 0)\, d\Delta_n, \quad \phi_t = \int_0^{\delta_t} T_t(0, \Delta_t)\, d\Delta_t. \tag{5}$$

- The normal and tangential tractions are maximum when the separations reach the critical opening displacements ($\delta_{nc}$, $\delta_{tc}$),

$$\left.\frac{\partial T_n}{\partial \Delta_n}\right|_{\Delta_n=\delta_{nc}} = 0, \quad \left.\frac{\partial T_t}{\partial \Delta_t}\right|_{\Delta_t=\delta_{tc}} = 0. \tag{6}$$

- The maximum tractions correspond to the cohesive strengths ($\sigma_{max}$, $\tau_{max}$),

$$T_n(\delta_{nc}, 0) = \sigma_{max}, \quad T_t(0, \delta_{tc}) = \tau_{max}. \tag{7}$$

- The shape parameter indices ($\alpha$, $\beta$) are introduced to characterize material softening responses, e.g. brittle, plateau and quasi-brittle.

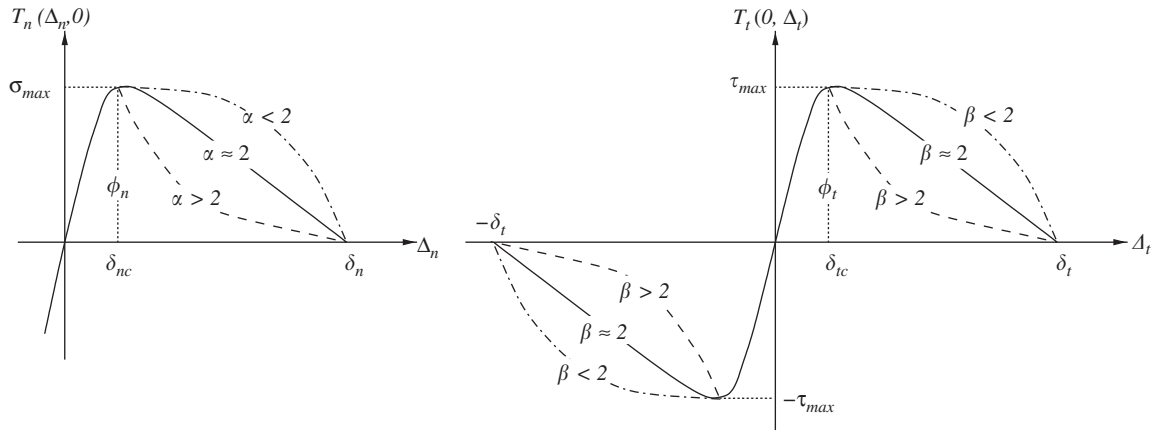


**Fig. 2.** Fracture boundary conditions for the unified mixed-mode potential.

Based on these physical macroscopic fracture parameters, the potential for mixed-mode fracture, called the PPR potential, is expressed as

$$\Psi(\Delta_n,\Delta_t)=\min(\phi_n,\phi_t)+\left[\Gamma_n\left(1-\frac{\Delta_n}{\delta_n}\right)^{\alpha}\left(\frac{m}{\alpha}+\frac{\Delta_n}{\delta_n}\right)^{m}+\langle\phi_n-\phi_t\rangle\right]\times\left[\Gamma_t\left(1-\frac{|\Delta_t|}{\delta_t}\right)^{\beta}\left(\frac{n}{\beta}+\frac{|\Delta_t|}{\delta_t}\right)^{n}+\langle\phi_t-\phi_n\rangle\right]. \tag{8}$$

The gradients of the PPR potential lead directly to the traction vector,

$$\begin{aligned}T_n(\Delta_n,\Delta_t)&=\frac{\Gamma_n}{\delta_n}\left[m\left(1-\frac{\Delta_n}{\delta_n}\right)^{\alpha}\left(\frac{m}{\alpha}+\frac{\Delta_n}{\delta_n}\right)^{m-1}-\alpha\left(1-\frac{\Delta_n}{\delta_n}\right)^{\alpha-1}\left(\frac{m}{\alpha}+\frac{\Delta_n}{\delta_n}\right)^{m}\right]\\&\quad\times\left[\Gamma_t\left(1-\frac{|\Delta_t|}{\delta_t}\right)^{\beta}\left(\frac{n}{\beta}+\frac{|\Delta_t|}{\delta_t}\right)^{n}+\langle\phi_t-\phi_n\rangle\right],\\T_t(\Delta_n,\Delta_t)&=\frac{\Gamma_t}{\delta_t}\left[n\left(1-\frac{|\Delta_t|}{\delta_t}\right)^{\beta}\left(\frac{n}{\beta}+\frac{|\Delta_t|}{\delta_t}\right)^{n-1}-\beta\left(1-\frac{|\Delta_t|}{\delta_t}\right)^{\beta-1}\left(\frac{n}{\beta}+\frac{|\Delta_t|}{\delta_t}\right)^{n}\right]\\&\quad\times\left[\Gamma_n\left(1-\frac{\Delta_n}{\delta_n}\right)^{\alpha}\left(\frac{m}{\alpha}+\frac{\Delta_n}{\delta_n}\right)^{m}+\langle\phi_n-\phi_t\rangle\right]\frac{\Delta_t}{|\Delta_t|},\end{aligned} \tag{9}$$

where $\langle\cdot\rangle$ is the *Macaulay bracket*, i.e.

$$\langle x\rangle=\begin{cases}0 & (x<0),\\ x & (x\geqslant 0).\end{cases} \tag{10}$$

The normal and tangential tractions satisfy basic symmetry and anti-symmetry requirements (with respect to $\Delta_t$), i.e.

$$T_n(\Delta_n,\Delta_t)=T_n(\Delta_n,-\Delta_t),\quad T_t(\Delta_n,\Delta_t)=-T_t(\Delta_n,-\Delta_t), \tag{11}$$

respectively. Notice that the value of $T_t(\Delta_n,\Delta_t)$ at $\Delta_t=0$ exists in the limit sense, i.e.

$$\lim_{\Delta_t\to 0^+}T_t(\Delta_n,\Delta_t)=0,\quad \lim_{\Delta_t\to 0^-}T_t(\Delta_n,\Delta_t)=0. \tag{12}$$

The eight characteristic parameters ($\Gamma_n$, $\Gamma_t$; $m$, $n$; $\delta_n$, $\delta_t$; $\alpha$, $\beta$) in the potential function are determined by satisfying the boundary conditions of macroscopic fracture. The energy constants, $\Gamma_n$ and $\Gamma_t$, are related to modes I and II fracture energy, which satisfy the boundary conditions of the fracture energies (5). When modes I and II fracture energy are different, one obtains the energy constants

$$\Gamma_n=(-\phi_n)^{\langle\phi_n-\phi_t\rangle/(\phi_n-\phi_t)}\left(\frac{\alpha}{m}\right)^{m},\quad \Gamma_t=(-\phi_t)^{\langle\phi_t-\phi_n\rangle/(\phi_t-\phi_n)}\left(\frac{\beta}{n}\right)^{n}\quad \text{for}\,(\phi_n\neq\phi_t). \tag{13}$$

If modes I and II fracture energy are the same, the energy constants are simplified as

$$\Gamma_n=-\phi_n\left(\frac{\alpha}{m}\right)^{m},\qquad \Gamma_t=\left(\frac{\beta}{n}\right)^{n}\quad \text{for}\,(\phi_n=\phi_t). \tag{14}$$

The non-dimensional exponents, $m$ and $n$, are evaluated by the boundary conditions of the critical separations (6) and the initial slope indicators ($\lambda_n$, $\lambda_t$),

$$m=\frac{\alpha(\alpha-1)\lambda_n^2}{(1-\alpha\lambda_n^2)},\quad n=\frac{\beta(\beta-1)\lambda_t^2}{(1-\beta\lambda_t^2)}. \tag{15}$$

The initial slope indicators are defined as the ratio of the critical crack opening width to the final crack opening width, i.e.

$$\lambda_n=\delta_{nc}/\delta_n,\quad \lambda_t=\delta_{tc}/\delta_t. \tag{16}$$

The initial slope indicators are introduced to control elastic behavior, which is eliminated in a constitutive model of extrinsic cohesive surface elements. Smaller values of $\lambda_n$, $\lambda_t$ (or $\delta_n$, $\delta_t$) result in the higher initial slope, and decrease artificial elastic deformation. Therefore, $\lambda_n$ and $\lambda_t$ are generally selected to be "small" values within the range of numerical stability for the intrinsic cohesive zone model.

The length scale parameters ($\delta_n$ and $\delta_t$) are the final normal and tangential crack opening widths whose boundary conditions (3, 4) are already satisfied by the potential function itself. The values of the final crack opening widths are determined by considering the boundary conditions of fracture energy (5) and of the cohesive strength (7),

$$\begin{aligned}\delta_n&=\frac{\phi_n}{\sigma_{max}}\alpha\lambda_n(1-\lambda_n)^{\alpha-1}\left(\frac{\alpha}{m}+1\right)\left(\frac{\alpha}{m}\lambda_n+1\right)^{m-1},\\ \delta_t&=\frac{\phi_t}{\tau_{max}}\beta\lambda_t(1-\lambda_t)^{\beta-1}\left(\frac{\beta}{n}+1\right)\left(\frac{\beta}{n}\lambda_t+1\right)^{n-1}.\end{aligned} \tag{17}$$

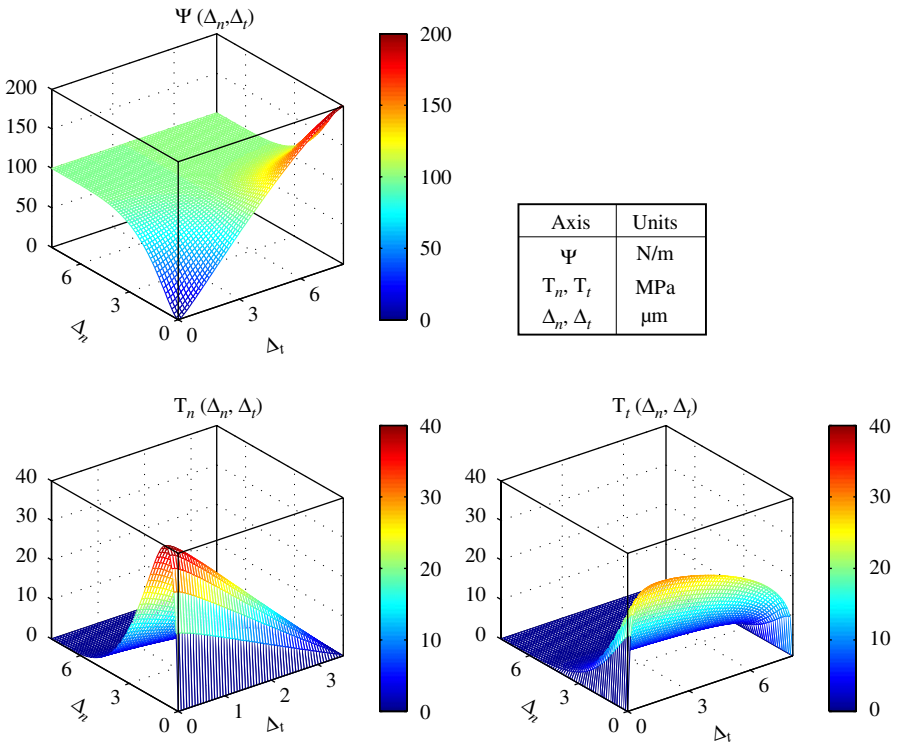


**Fig. 3.** Unified mixed-mode potential (PPR) and its gradients for the intrinsic cohesive zone model with $\phi_n = 100\,N/m$, $\phi_t = 200\,N/m$, $\sigma_{max} = 40\,MPa$, $\tau_{max} = 30\,MPa$, $\alpha = 5$, $\beta = 1.3$, $\lambda_n = 0.1$ and $\lambda_t = 0.2$.

The non-dimensional shape parameter indices ($\alpha$, $\beta$) are introduced because the specific shape of the cohesive zone model can significantly affect results of the fracture analysis (see, for example, Volokh, 2004; Alfano, 2006; Song et al., 2008). If the shape parameter indices are equal to two, the order of the potential function is approximately two. Then, the resulting gradient of the potential represents almost a linearly decreasing cohesive relationship. When the shape parameters are less than two, the gradient of the potential demonstrates a concave softening shape, which can represent a plateau-type function. If the shape parameter indices are chosen as larger values, the cohesive interaction has a convex shape.

In summary, the potential function for mixed-mode cohesive fracture is developed by satisfying the boundary conditions of macroscopic fracture. The unified potential and its gradients are plotted in Fig. 3. The plotted potential represents different fracture energies (e.g. $\phi_n = 100\,N/m$, $\phi_t = 200\,N/m$), cohesive strengths (e.g. $\sigma_{max} = 40\,MPa$, $\tau_{max} = 30\,MPa$), cohesive interactions (e.g. $\alpha = 5$, $\beta = 1.3$) and initial slope indicators (e.g. $\lambda_n = 0.1$, $\lambda_t = 0.2$). The mode I cohesive relationship illustrates fracture behavior of a typical quasi-brittle material, while the mode II cohesive relationship describes a plateau-type behavior. The potential is also applicable when the mode I fracture energy is greater than mode II fracture energy because the potential is explicitly derived by using the symmetric boundary conditions for modes I and II.

### 2.2. Cohesive interaction (softening) region

The proposed potential is a continuous polynomial function. Exponential potentials result in an infinite final crack opening width, while the polynomial-based potential provides a finite final crack opening width. Because of this fact, the polynomial potential is only valid in the defined softening region. For example, mathematically the unbounded polynomial potential provides non-zero traction even after a physical separation is greater than a final crack opening width. Therefore, we must define a region for each cohesive interaction ($T_n$, $T_t$) in terms of a set of material-derived final crack opening widths (e.g. $\delta_n$, $\delta_t$) and calculated conjugate final crack opening widths (e.g. $\bar{\delta}_n$, $\bar{\delta}_t$).

The cohesive interaction region is defined as a rectangular region for each cohesive interaction in conjunction with the final crack opening widths ($\delta_n$, $\delta_t$) and the conjugate final crack opening widths ($\bar{\delta}_n$, $\bar{\delta}_t$) as shown in Fig. 4. For the normal cohesive interaction ($T_n$), one border of the softening region is the normal final crack opening width ($\delta_n$). If the normal separation is greater than the normal final crack opening width ($\Delta_n > \delta_n$), the normal traction ($T_n$) is set to zero. The other border of the softening region is the tangential conjugate final crack opening width ($\bar{\delta}_t$). If the tangential separation is

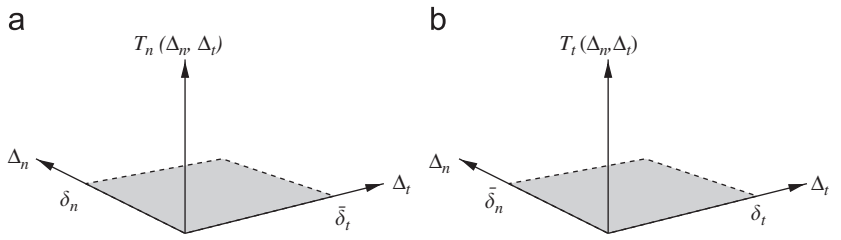


**Fig. 4.** Description of each cohesive interaction ($T_n$, $T_t$) region defined by the final crack opening widths ($\delta_n$, $\delta_t$) and the conjugate final crack opening widths ($\bar{\delta}_n$, $\bar{\delta}_t$): (a) $T_n$ versus ($\delta_n, \bar{\delta}_t$) space and (b) $T_t$ versus ($\bar{\delta}_n, \delta_t$) space.

greater than the tangential conjugate final crack opening width ($\Delta_t > \bar{\delta}_t$), the normal traction is also set to be zero. The value of the tangential conjugate final crack opening width ($\bar{\delta}_t$) is obtained by satisfying the boundary condition of $T_n(\Delta_n, \bar{\delta}_t) = 0$. Since $\Delta_n$ is an arbitrary separation, the tangential conjugate final crack opening width ($\Delta_t = \bar{\delta}_t$) is the solution of the nonlinear function

$$f_t(\Delta_t) = \Gamma_t\left(1 - \frac{|\Delta_t|}{\delta_t}\right)^{\beta}\left(\frac{n}{\beta} + \frac{|\Delta_t|}{\delta_t}\right)^{n} + \langle \phi_t - \phi_n \rangle = 0. \tag{18}$$

The uniqueness of the solution between 0 and $\delta_t$ is proved in the following way. When the mode II fracture energy ($\phi_t$) is greater than the mode I fracture energy ($\phi_n$), $f_t(0) = -\phi_n < 0$ and $f_t(\delta_t) = \phi_t - \phi_n > 0$. Because $f_t'(\Delta_t)$ is always positive within the range of $0 \leqslant \Delta_t \leqslant \delta_t$, the function $f_t(\Delta_t)$ has a single solution between 0 and $\delta_t$. Additionally, when $\phi_t$ is not greater than $\phi_n$, the solution of a function $f_t(\Delta_t)$ is the same as the tangential final crack opening width, i.e. $\bar{\delta}_t = \delta_t$.

Accordingly, the cohesive interaction region for the tangential traction is defined by the tangential final crack opening width ($\delta_t$) and the normal conjugate final crack opening width ($\bar{\delta}_n$). The normal conjugate final crack opening width ($\Delta_n = \bar{\delta}_n$) is the solution of the nonlinear function

$$f_n(\Delta_n) = \Gamma_n\left(1 - \frac{\Delta_n}{\delta_n}\right)^{\alpha}\left(\frac{m}{\alpha} + \frac{\Delta_n}{\delta_n}\right)^{m} + \langle \phi_n - \phi_t \rangle = 0. \tag{19}$$

The derivative of $f_n(\Delta_n)$ is positive within the rage of $0 \leqslant \Delta_n \leqslant \delta_n$ when $\phi_n$ is greater than $\phi_t$. Then, because $f_n(0) < 0$ and $f_n(\delta_n) > 0$, the function $f_n(\Delta_n)$ has a single solution between 0 and $\delta_n$. When $\phi_n$ is not greater than $\phi_t$, the solution of a function $f_n(\Delta_n)$ is the normal final crack opening width, i.e. $\bar{\delta}_n = \delta_n$.

In summary, the normal cohesive interaction ($T_n$) is defined within the normal final crack opening with ($\delta_n$) and the tangential conjugate final crack opening width ($\bar{\delta}_t$) space (Fig. 4(a)). The tangential cohesive interaction ($T_t$) is defined within the tangential final crack opening width ($\delta_t$) and the normal conjugate final crack opening with ($\bar{\delta}_n$) space (Fig. 4(b)). The introduction of the conjugate final crack opening widths ($\bar{\delta}_n$, $\bar{\delta}_t$) guarantees that a non-zero traction will not occur when load bearing capacity is lost.

### 2.3. Extension to the extrinsic cohesive zone model

The PPR potential function is extended for the case of the extrinsic cohesive zone models. In this case, cohesive surface elements are adaptively inserted on the basis of an external crack initiation criterion. The potential function excludes the elastic behavior (or initial slope) in the cohesive interactions. The limit of initial slope indicators in the PPR potential function ($\lambda_n \to 0$ and $\lambda_t \to 0$) eliminates the initial slope indicators ($\lambda_n$, $\lambda_t$) and the exponents ($m$, $n$) from the resulting expression. Thus one obtains the potential function for the extrinsic cohesive zone model expressed as

$$\Psi(\Delta_n, \Delta_t) = \min(\phi_n, \phi_t) + \left[\Gamma_n\left(1 - \frac{\Delta_n}{\delta_n}\right)^{\alpha} + \langle \phi_n - \phi_t \rangle\right]\left[\Gamma_t\left(1 - \frac{|\Delta_t|}{\delta_t}\right)^{\beta} + \langle \phi_t - \phi_n \rangle\right]. \tag{20}$$

The gradient of the potential leads to the normal and tangential tractions along the fractured surface,

$$\begin{aligned} T_n(\Delta_n, \Delta_t) &= -\alpha\frac{\Gamma_n}{\delta_n}\left(1 - \frac{\Delta_n}{\delta_n}\right)^{\alpha-1}\left[\Gamma_t\left(1 - \frac{|\Delta_t|}{\delta_t}\right)^{\beta} + \langle \phi_t - \phi_n \rangle\right], \\ T_t(\Delta_n, \Delta_t) &= -\beta\frac{\Gamma_t}{\delta_t}\left(1 - \frac{|\Delta_t|}{\delta_t}\right)^{\beta-1}\left[\Gamma_n\left(1 - \frac{\Delta_n}{\delta_n}\right)^{\alpha} + \langle \phi_n - \phi_t \rangle\right]\frac{\Delta_t}{|\Delta_t|}. \end{aligned} \tag{21}$$

The normal and tangential tractions satisfy the symmetry and anti-symmetry requirements, respectively, according to Eq. (11). The tangential traction provides a finite value at the initiation point ($\Delta_t = 0$), and therefore introduces the

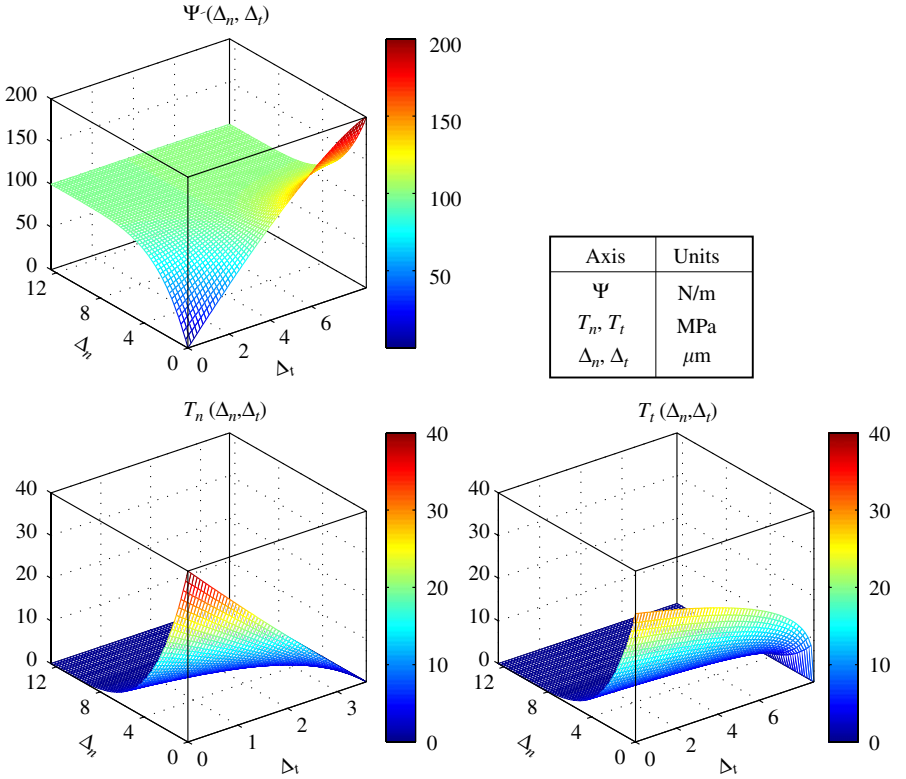


**Fig. 5.** Proposed potential and its gradients for the extrinsic cohesive zone model with $\phi_{\mathrm{n}} = 100\,\mathrm{N/m}$, $\phi_{\mathrm{t}} = 200\,\mathrm{N/m}$, $\sigma_{\max} = 40\,\mathrm{MPa}$, $\tau_{\max} = 30\,\mathrm{MPa}$, $\alpha = 5$ and $\beta = 1.3$.

discontinuity, i.e.

$$\lim_{\Delta_{\mathrm{t}}\to 0^{+}} T_{\mathrm{t}}(\Delta_{\mathrm{n}},\Delta_{\mathrm{t}}) = -\beta\frac{\Gamma_{\mathrm{t}}}{\delta_{\mathrm{t}}}\left[\Gamma_{\mathrm{n}}\left(1-\frac{\Delta_{\mathrm{n}}}{\delta_{\mathrm{n}}}\right)^{\alpha} + \langle\phi_{\mathrm{n}}-\phi_{\mathrm{t}}\rangle\right],$$
$$\lim_{\Delta_{\mathrm{t}}\to 0^{-}} T_{\mathrm{t}}(\Delta_{\mathrm{n}},\Delta_{\mathrm{t}}) = \beta\frac{\Gamma_{\mathrm{t}}}{\delta_{\mathrm{t}}}\left[\Gamma_{\mathrm{n}}\left(1-\frac{\Delta_{\mathrm{n}}}{\delta_{\mathrm{n}}}\right)^{\alpha} + \langle\phi_{\mathrm{n}}-\phi_{\mathrm{t}}\rangle\right], \tag{22}$$

which corresponds to a feature of the extrinsic cohesive zone models.

The normal and tangential tractions are defined in a softening region associated with the final crack opening width $(\delta_{\mathrm{n}}, \delta_{\mathrm{t}})$ and the conjugate final crack opening width $(\bar{\delta}_{\mathrm{n}}, \bar{\delta}_{\mathrm{t}})$. The final crack opening widths are expressed as

$$\delta_{\mathrm{n}} = \alpha\phi_{\mathrm{n}}/\sigma_{\max}, \quad \delta_{\mathrm{t}} = \beta\phi_{\mathrm{t}}/\tau_{\max}, \tag{23}$$

which are associated with the fracture boundary conditions, such as the fracture energies and the cohesive strengths. The conjugate final crack opening widths $(\bar{\delta}_{\mathrm{n}}, \bar{\delta}_{\mathrm{t}})$ are given by

$$\bar{\delta}_{\mathrm{n}} = \delta_{\mathrm{n}} - \delta_{\mathrm{n}}\left(\frac{\langle\phi_{\mathrm{n}}-\phi_{\mathrm{t}}\rangle}{\phi_{\mathrm{n}}}\right)^{1/\alpha}, \quad \bar{\delta}_{\mathrm{t}} = \delta_{\mathrm{t}} - \delta_{\mathrm{t}}\left(\frac{\langle\phi_{\mathrm{t}}-\phi_{\mathrm{n}}\rangle}{\phi_{\mathrm{t}}}\right)^{1/\beta}, \tag{24}$$

which satisfy the conditions of $T_{\mathrm{t}}(\bar{\delta}_{\mathrm{n}},\Delta_{\mathrm{t}}) = 0$ and $T_{\mathrm{n}}(\Delta_{\mathrm{n}},\bar{\delta}_{\mathrm{t}}) = 0$, respectively. The energy constants are expressed as

$$\Gamma_{\mathrm{n}} = (-\phi_{\mathrm{n}})^{\langle\phi_{\mathrm{n}}-\phi_{\mathrm{t}}\rangle/(\phi_{\mathrm{n}}-\phi_{\mathrm{t}})}, \quad \Gamma_{\mathrm{t}} = (-\phi_{\mathrm{t}})^{\langle\phi_{\mathrm{t}}-\phi_{\mathrm{n}}\rangle/(\phi_{\mathrm{t}}-\phi_{\mathrm{n}})} \quad (\phi_{\mathrm{n}}\neq\phi_{\mathrm{t}}) \tag{25}$$

for the different fracture energies. If the fracture energies are the same, one obtains the energy constants,

$$\Gamma_{\mathrm{n}} = -\phi_{\mathrm{n}}, \quad \Gamma_{\mathrm{t}} = 1 \quad (\phi_{\mathrm{n}} = \phi_{\mathrm{t}}). \tag{26}$$

With the same fracture parameters as illustrated in Fig. 3, the potential for the extrinsic cohesive zone model is plotted in Fig. 5. The initial slope is excluded, and the traction discontinuity is introduced at zero separation. The shape of the potential is concave because the potential is only associated to behaviors which occur after the bifurcation point (cf. Fig. 1). In summary, rather than providing infinite slope, the cohesive interactions for the extrinsic cohesive zone model are derived by taking the limit from the potential function. Thus, the discontinuities are naturally introduced at crack initiation.

### 2.4. Remarks

The PPR potential for mixed-mode cohesive fracture is associated with physical macroscopic fracture parameters, i.e. fracture energies ($\phi_n$, $\phi_t$), cohesive strengths ($\sigma_{max}$, $\tau_{max}$), softening curves shape ($\alpha$, $\beta$) and the initial slope indicators ($\lambda_n$, $\lambda_t$). In addition, the potential-based model for the extrinsic cohesive zone models is within the same framework as for the intrinsic cohesive zone model. The characteristics of the proposed potential are summarized as follows:

- Differentiates fracture energies ($\phi_n$, $\phi_t$) and cohesive strengths ($\sigma_{max}$, $\tau_{max}$) in fracture modes I and II.
- Suitable for various material softening responses, e.g. "ductile" (plateau), brittle, and quasi-brittle, because of the shape parameters ($\alpha$, $\beta$).
- The normal and tangential tractions ($T_n$, $T_t$) are defined by the final crack opening widths ($\delta_n$, $\delta_t$) and the conjugate final crack opening widths ($\bar{\delta}_n$, $\bar{\delta}_t$).
- The initial slope indicators ($\lambda_n$, $\lambda_t$) control the artificial elastic behavior in the intrinsic cohesive zone model.
- The limit of the initial slope indicators results in the potential function for the extrinsic cohesive zone model.
- Obeys the symmetry condition, i.e. an exact differential with $\partial T_n/\partial \Delta_t = \partial T_t/\partial \Delta_n$. The values of the differential at $\Delta_t = 0$ exists in the limit sense.
- The normal negative displacements are penalized to prevent material self-penetration. Alternative approaches, involving contact mechanics, may also be used.
- Unloading/reloading are handled independently of the potential.
- Utilizes polynomial function to avoid the infinite final crack opening width of the exponential potential.

## 3. Path dependence of work-of-separation

Energy dissipated due to the fracture depends on separation paths when the mode I fracture energy ($\phi_n$) is different from the mode II fracture energy ($\phi_t$). In order to evaluate the energy variation with respect to a path, the work-of-separation ($W_{sep}$) is defined as follows:

$$W_{sep} = \int_\Gamma T_n(\Delta_n, \Delta_t)\,d\Delta_n + \int_\Gamma T_t(\Delta_n, \Delta_t)\,d\Delta_t, \tag{27}$$

where $\Gamma$ is a separation path. The first term in the work-of-separation expression is the work done by the normal traction ($W_n$), while the second term in the expression is the work done by the tangential traction ($W_t$). In this study, we compare

**Table 2**
Fracture parameters for the unified potential-based model (PPR)

| $\phi_n$ (N/m) | $\phi_t$ (N/m) | $\sigma_{max}$ (MPa) | $\tau_{max}$ (MPa) | $\alpha$ | $\beta$ | $\lambda_n$ | $\lambda_t$ |
|---|---|---|---|---|---|---|---|
| 100 | 200 | 3 | 12 | 3 | 3 | 0.01 | 0.01 |

**Table 3**
Fracture parameters for the model by Xu and Needleman (1993)

| $\phi_n$ (N/m) | $\phi_t$ (N/m) | $\sigma_{max}$ (MPa) | $\tau_{max}$ (MPa) | $r$ |
|---|---|---|---|---|
| 100 | 200 | 3 | 12 | 0.5 |

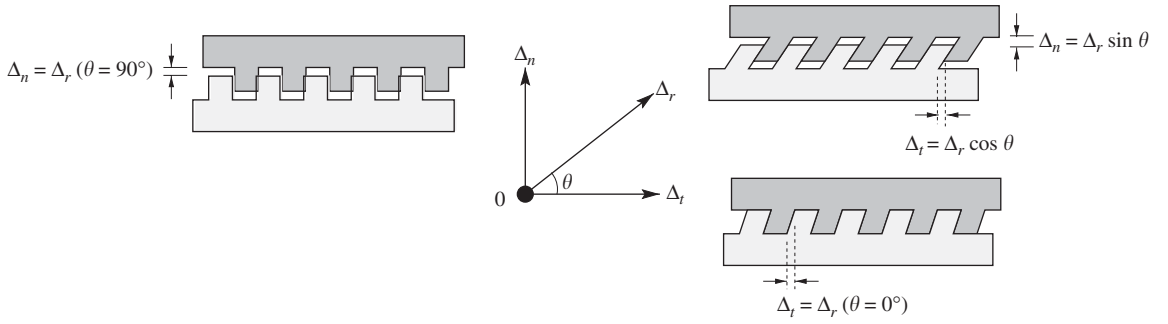


**Fig. 6.** Proportional separation path ($\Delta_r$) with the separation angle ($\theta$).

energy variations of the unified potential-based model (PPR) with those of the model by Xu and Needleman (1993) for proportional separation paths and non-proportional paths. Tables 2 and 3 illustrate the fracture parameters utilized in this investigation. The mode I fracture energy ($\phi_n$) is arbitrarily selected as 100 N/m, and the mode II fracture energy ($\phi_t$) as 200 N/m.

### 3.1. Proportional separation

The proportional separation path is associated with the separation angle ($\theta$), as shown in Fig. 6. The work-of-separation for the unified potential-based model is expressed in terms of $\Delta_r$ and $\theta$,

$$W_{sep} = \int_0^{\delta_r} T_n(\Delta_r \sin\theta, \Delta_r \cos\theta) \sin\theta \, d\Delta_r + \int_0^{\delta_r} T_t(\Delta_r \sin\theta, \Delta_r \cos\theta) \cos\theta \, d\Delta_r, \tag{28}$$

where $\delta_r = \sqrt{\delta_n^2 + \delta_t^2}$. When the separation angle is 90°, the material experiences pure mode I fracture for which the work-of-separation is equal to the mode I fracture energy. When $\theta = 0°$, the material experiences pure mode II fracture for which the work-of-separation is the same as the mode II fracture energy. For the intermediate angles ($0° < \theta < 90°$), i.e. mixed-mode fracture, the work-of-separation is between the pure mode I and the pure mode II fracture energies.

Fig. 7(a)–(c) demonstrate the analytical variation of the work-of separation ($W_{sep}$), the work done by the normal traction ($W_n$), and the work done by the tangential traction ($W_t$) with respect to the change of the proportional angle, respectively. When the separation angle is 90°, i.e. mode I fracture, $W_{sep}$ and $W_n$ increase from 0 to the mode I fracture energy (100 N/m) with the increase of $\Delta_r$, while $W_t$ remains zero. When $\theta$ is equal to 0°, i.e. mode II fracture, $W_{sep}$ and $W_t$ change from 0 to

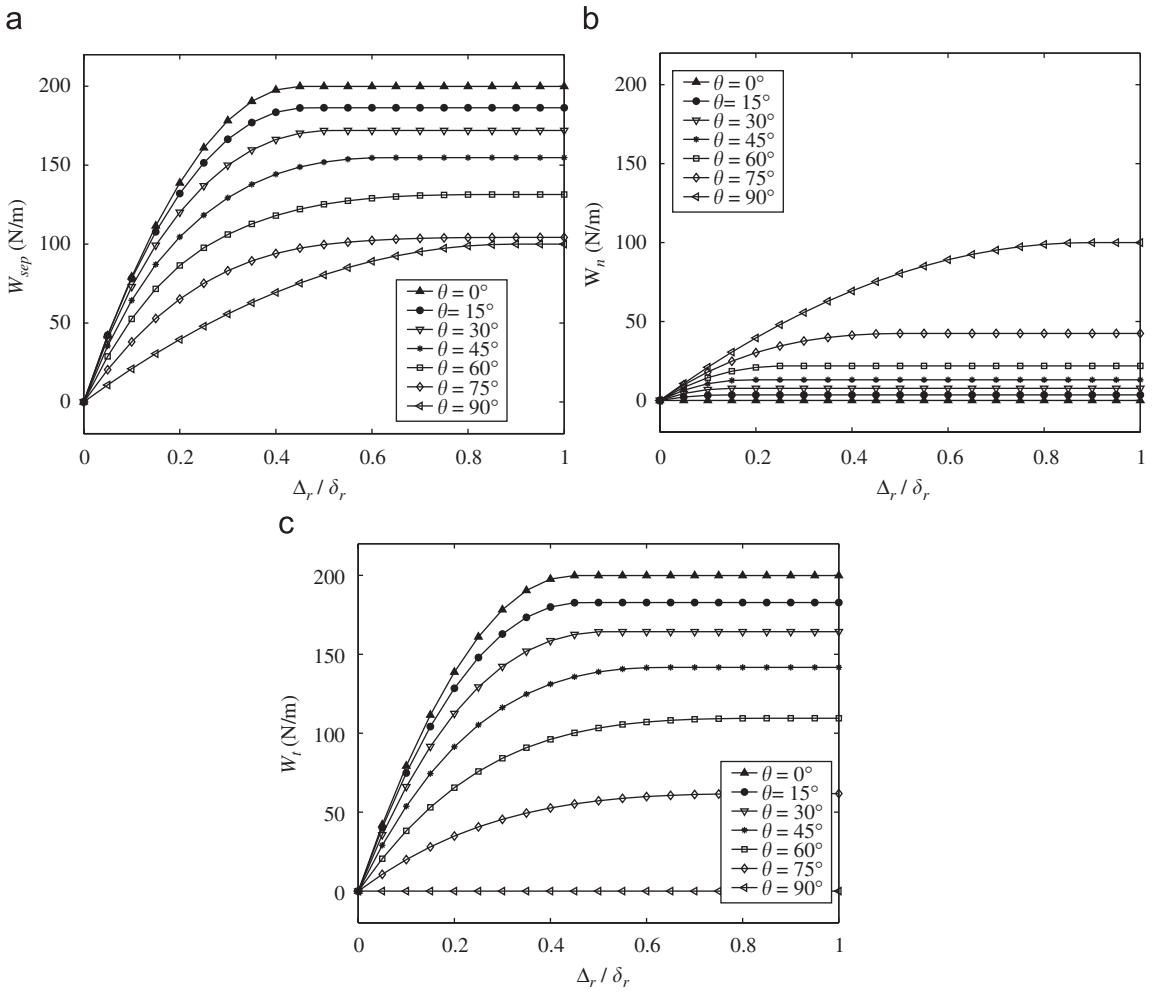


**Fig. 7.** The PPR potential-based method: (a) work-of-separation, (b) work done by the normal traction and (c) work done by the tangential traction with respect to the change of the proportional angle, $\theta$.

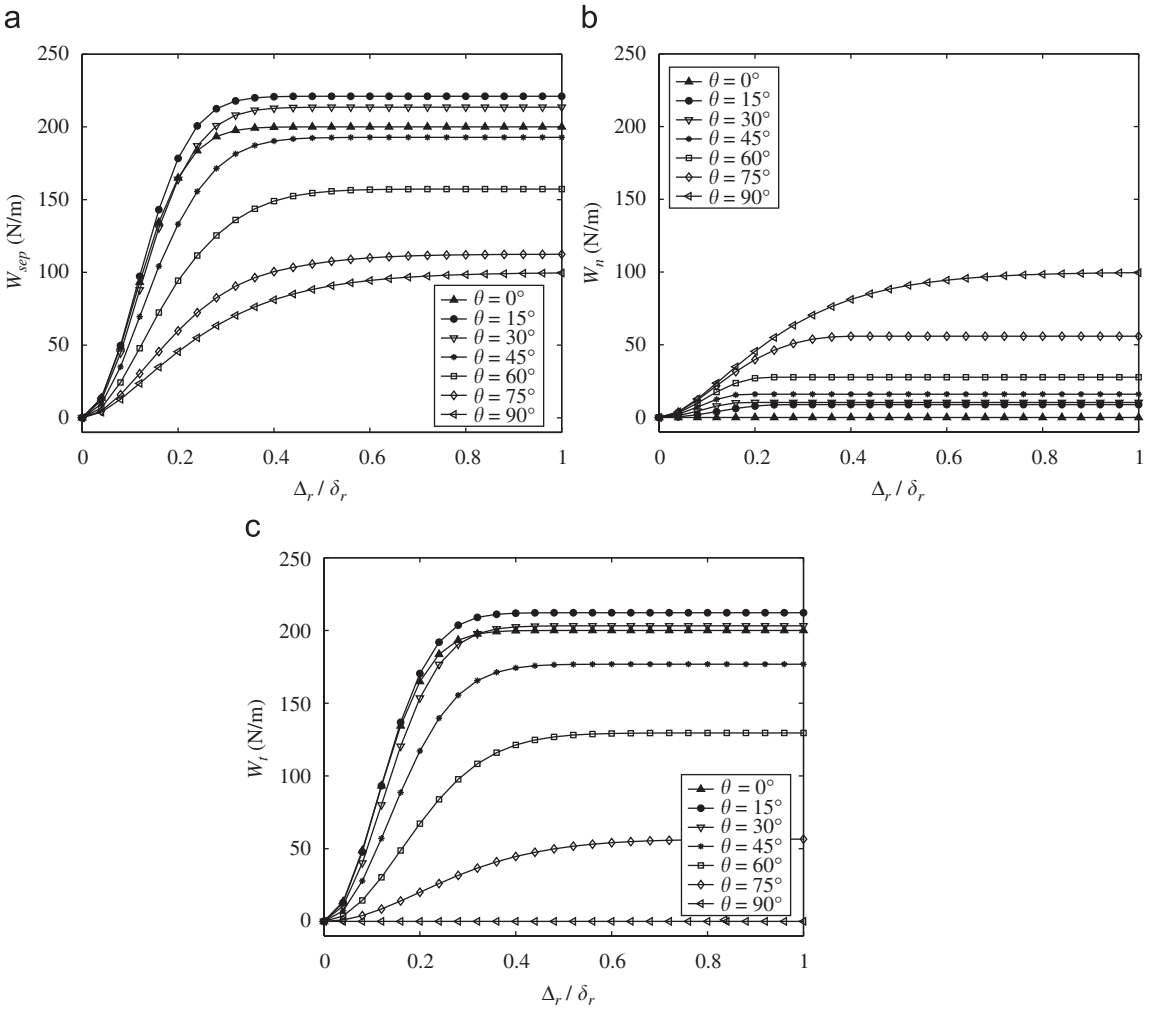


**Fig. 8.** Xu and Needleman (1993) exponential potential: (a) work-of-separation, (b) work done by the normal traction and (c) work done by the tangential traction with respect to the change of the proportional angle, $\theta$.

the mode II fracture energy (200 N/m) with the increase of $\Delta_r$, while $W_n$ remains zero. For the intermediate angles ($0^\circ < \theta < 90^\circ$), i.e. mixed-mode fracture, $W_{sep}$, $W_n$ and $W_t$ vary monotonically including both the mode I and II fracture behavior.

Accordingly, for the cohesive fracture model by Xu and Needleman (1993), the work-of-separation expression is given as (cf. Eq. (28))

$$W_{sep} = \int_0^\infty T_n(\Delta_r \sin\theta, \Delta_r \cos\theta) \sin\theta \, d\Delta_r + \int_0^\infty T_t(\Delta_r \sin\theta, \Delta_r \cos\theta) \cos\theta \, d\Delta_r. \tag{29}$$

Fig. 8 illustrates the variation of $W_{sep}$, $W_n$ and $W_t$ with respect to the separation angles. When the separation angle is $0^\circ$, $W_{sep}$ and $W_t$ reach the mode II fracture energy (200 N/m), and $W_n$ keeps zero. Increasing the separation angle results in the increase of the work done by the normal traction, and the decrease of $W_{sep}$ and $W_t$. However, both $W_{sep}$ and $W_t$ increase monotonically with respect to the increase of the separation angle from $0^\circ$ to $15^\circ$ (see Fig. 8(a) and (c)), but not with respect to $30^\circ$ in this example. The work-of-separation does not change monotonically under mixed-mode fracture condition, and thus the exponential potential model does not guarantee the consistency of the cohesive constitutive model.

### 3.2. Non-proportional separation

For non-proportional separation paths, one could assume that material particles experience normal separation until $\Delta_n = \Delta_{n,max}$ and then the complete tangential separation occurs, i.e. path 1 in Fig. 9(a). The other path is that material

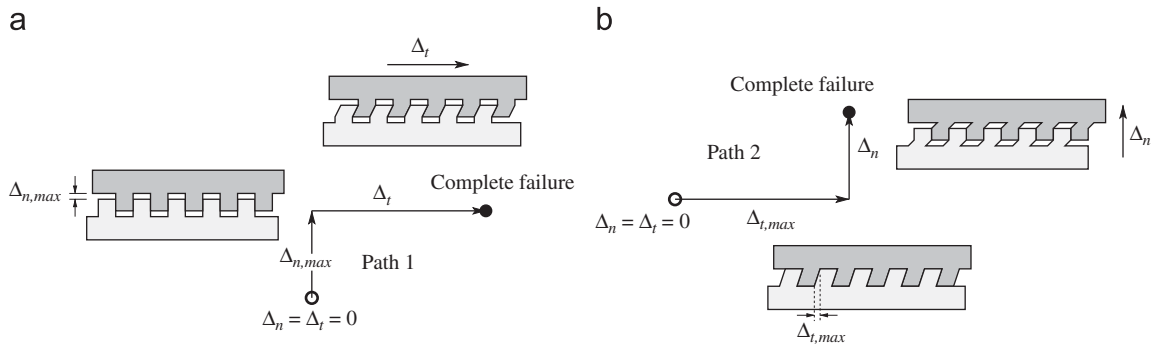


**Fig. 9.** Two arbitrary separation paths for the material debonding process: (a) non-proportional **Path 1** and (b) non-proportional **Path 2**.

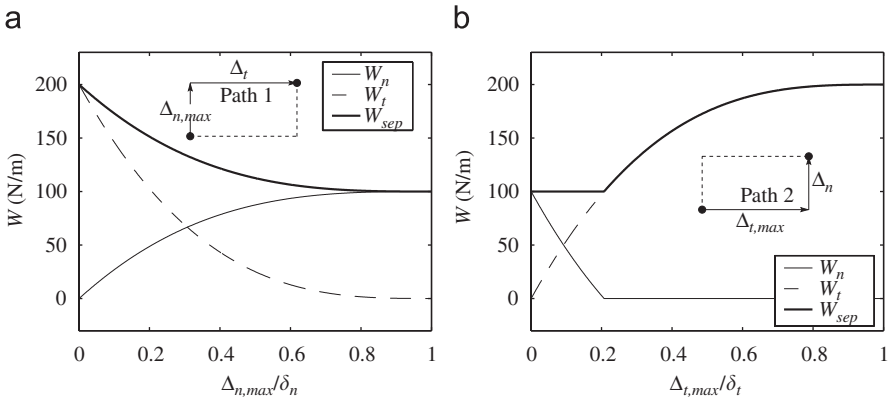


**Fig. 10.** The PPR potential-based method: variation of the work-of-separation for the case of $\phi_n < \phi_t$ ($\phi_n = 100\,\mathrm{N/m}$, $\phi_t = 200\,\mathrm{N/m}$): (a) non-proportional **Path 1** and (b) non-proportional **Path 2**.

separates along the tangential direction first until $\Delta_t = \Delta_{t,max}$ and then the failure occurs along the normal direction, i.e. path 2 in Fig. 9(b). For the first path, the work-of-separation of the PPR model is evaluated by the following expression:

$$W_{sep} = \int_0^{\Delta_{n,max}} T_n(\Delta_n, 0)\, d\Delta_n + \int_0^{\delta_t} T_t(\Delta_{n,max}, \Delta_t)\, d\Delta_t. \tag{30}$$

Accordingly, the work-of-separation for the second path is expressed as

$$W_{sep} = \int_0^{\Delta_{t,max}} T_t(0, \Delta_t)\, d\Delta_t + \int_0^{\delta_n} T_n(\Delta_n, \Delta_{t,max})\, d\Delta_n. \tag{31}$$

Fig. 10 demonstrates the variation of the work-of-separation with respect to the two arbitrary separation paths. The mode I fracture energy is selected as 100 N/m and the mode II fracture energy as 200 N/m. The work done by the normal separation is indicated as a thin solid line while the work done by the tangential separation is given as a dashed line. For the first non-proportional path (Fig. 9(a)), $\Delta_{n,max} = 0$ represents the pure mode II failure while $\Delta_{n,max} = \delta_n$ describes the pure mode I failure. Then, the change of $\Delta_{n,max}$ from 0 to $\delta_n$ demonstrates the gradual change of the mode mixity from the mode II fracture to the mode I fracture. The work done ($W_t$) by the tangential traction, therefore, monotonically decreases from $\phi_t$ to 0, while the work done ($W_n$) by the normal traction gradually increases from 0 to $\phi_n$, as shown in Fig. 10(a). The work-of-separation ($W_{sep}$) monotonically varies from the value of $\phi_t$ to the value of $\phi_n$ by increasing $\Delta_{n,max}$ from 0 to $\delta_n$. In the path 2 (Fig. 9(b)), when $\Delta_{t,max}$ is zero, the separation path illustrates the pure mode I failure while $\Delta_{t,max} = \delta_t$ represents the pure mode II failure. The work-of-separation ($W_{sep}$) monotonically changes from the mode I fracture energy to the mode II fracture energy although there is a kink point as shown in Fig. 10(b).

The separation at the kink point corresponds to the tangential conjugate final crack opening width ($\Delta_{t,max} = \bar{\delta}_t$). When $\Delta_t$ is smaller than $\bar{\delta}_t$, the normal cohesive interaction is obtained by the derivative of the PPR potential with respect to the normal separation. When $\Delta_t$ is greater than $\bar{\delta}_t$, the normal cohesive interaction is set to zero. The normal cohesive interaction is then not smooth but piece-wise continuous at $\Delta_{t,max} = \bar{\delta}_t$ in this example. The integration of the normal cohesive interaction can also be piece-wise continuous at the same point. Therefore, the work done ($W_n$) by the normal

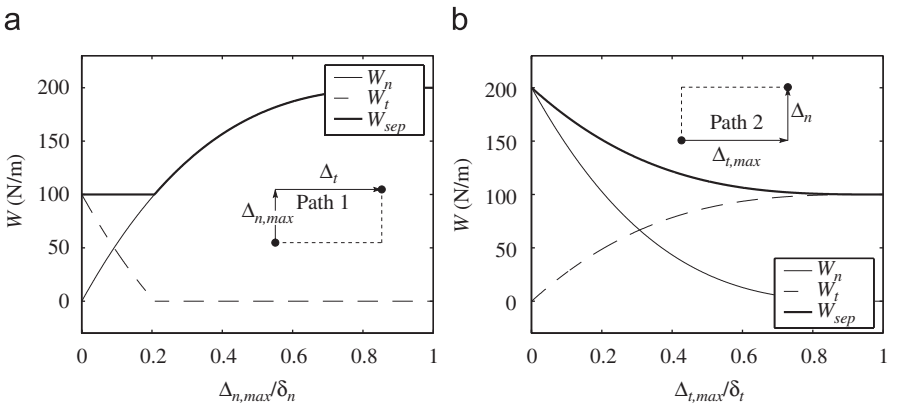


**Fig. 11.** The PPR potential-based method: variation of the work-of-separation for the case of $\phi_n > \phi_t$ ($\phi_n = 200\,\mathrm{N/m}$, $\phi_t = 100\,\mathrm{N/m}$): (a) non-proportional **Path 1** and (b) non-proportional **Path 2**.

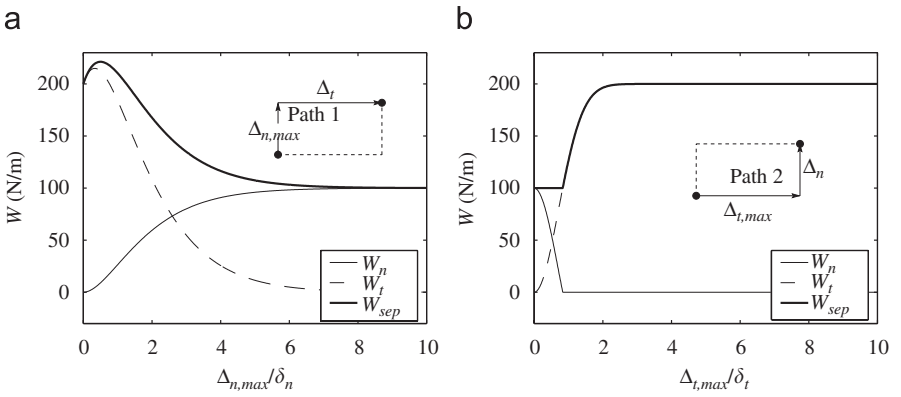


**Fig. 12.** Xu and Needleman (1993) exponential potential: variation of the work-of-separation for the case of $\phi_n < \phi_t$ ($\phi_n = 100\,\mathrm{N/m}$, $\phi_t = 200\,\mathrm{N/m}$ and $r = 0.5$): (a) non-proportional **Path 1** and (b) non-proportional **Path 2**.

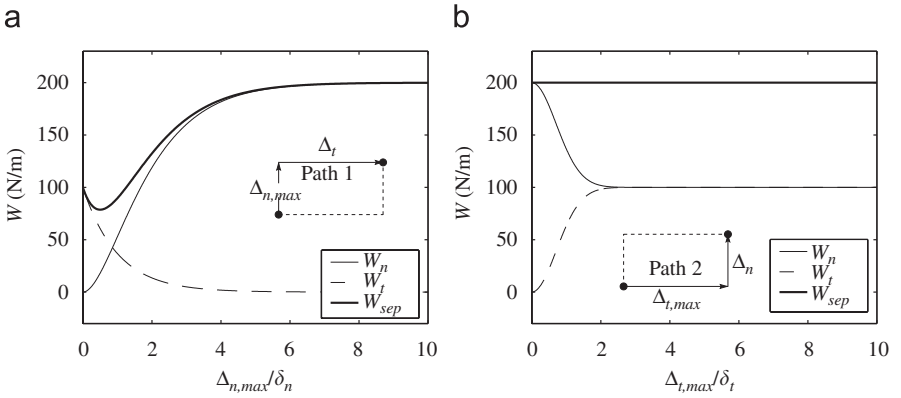


**Fig. 13.** Xu and Needleman (1993) exponential potential: variation of the work-of-separation for the case of $\phi_n > \phi_t$ ($\phi_n = 200\,\mathrm{N/m}$, $\phi_t = 100\,\mathrm{N/m}$ and $r = 0.5$) and (a) non-proportional **Path 1** and (b) non-proportional **Path 2**.

separation changes from $\phi_n$ to zero between $\Delta_{t,max} = 0$ (pure mode I) and $\Delta_{t,max} = \bar{\delta}_t$ (pure mode II), and demonstrates piece-wise continuity at $\Delta_{t,max} = \bar{\delta}_t$. As a result, the work-of-separation ($W_{sep} = W_n + W_t$) also have the kink point at the same location.

Additionally, similar energy variation is expected when the mode I fracture energy is greater than the mode II fracture energy (e.g. $\phi_n = 200\,\mathrm{N/m}$, $\phi_t = 100\,\mathrm{N/m}$), as shown in Fig. 11. This is because the potential function is based on the symmetric boundary conditions of fracture. The work-of-separation curve monotonically changes from one fracture mode

to the other fracture mode. The kink point occurs in the first separation path because the tangential cohesive interaction ($T_t$) is piece-wise continuous at $\Delta_{n,max} = \bar{\delta}_n$.

For the model by Xu and Needleman (1993), a similar investigation was implemented by van den Bosch et al. (2006). The work-of-separation for the first non-proportional path in Fig. 9(a) is expressed as

$$W_{sep} = \int_0^{\Delta_{n,max}} T_n(\Delta_n, 0)\, d\Delta_n + \int_0^{\infty} T_t(\Delta_{n,max}, \Delta_t)\, d\Delta_t. \tag{32}$$

The work-of-separation for the second path (Fig. 9(b)) is expressed as

$$W_{sep} = \int_0^{\Delta_{t,max}} T_t(0, \Delta_t)\, d\Delta_t + \int_0^{\infty} T_n(\Delta_n, \Delta_{t,max})\, d\Delta_n. \tag{33}$$

The work-of-separations for the two arbitrary separation paths are plotted in Figs. 12 and 13. Fig. 12 is the case when the mode II fracture energy is greater than the mode I fracture energy (e.g. $\phi_n = 100\,N/m$, $\phi_t = 200\,N/m$), and Fig. 13 is the case of $\phi_n > \phi_t$ (e.g. $\phi_n = 200\,N/m$, $\phi_t = 100\,N/m$). With respect to increasing the maximum normal separation ($\Delta_{n,max}$), the work-of-separation for the path 1 (Figs. 12(a) and 13(a)) does not monotonically vary from the mode I fracture energy to the mode II fracture energy. The second path in Fig. 12(b) demonstrates the monotonic variation of the work-of-separation with the change in the maximum tangential separation ($\Delta_{t,max}$). The kink point in Fig. 12(b) results from cutting off the negative normal traction region. In this example, when the tangential separation is greater than a certain value, the exponential potential leads to negative normal traction. Since the work done should always be positive, we assume that the normal cohesive interaction set to be zero within the negative traction range. Therefore, $W_n$ and $W_{sep}$ are not smooth but piece-wise continuous as shown in Fig. 12(b). Additionally, for the path 2 in Fig. 13(b), the work done by normal separation does not decrease to zero although material particles experience large shear separation.

## 4. Mixed-mode fracture verification

The PPR potential-based model for cohesive fracture is verified by simulating a mixed-mode fracture problem, the mixed-mode bending (MMB) test. The MMB test was developed by Reeder and Crews (1990) in order to investigate the fracture toughness variation with respect to the mode mixity. The test has been standardized by ASTM (2006). The configuration of an MMB test is the combination of the double cantilever beam test (mode I loading) and the end-notch flexure test (mode II loading) as shown in Fig. 14. Numerical simulations of the mixed-mode fracture are implemented by using the commercial software ABAQUS with a user-defined element (UEL) subroutine. The formulation of cohesive surface elements is derived by the virtual work formulation with the updated Lagrangian finite element discretization.

In this numerical verification, we simulate two hypothetical cases, one with the same fracture energy ($\phi_n = \phi_t = 1\,N/m$) and another with different fracture energies ($\phi_n = 1\,N/m$, $\phi_t = 2\,N/m$). The elastic modulus is

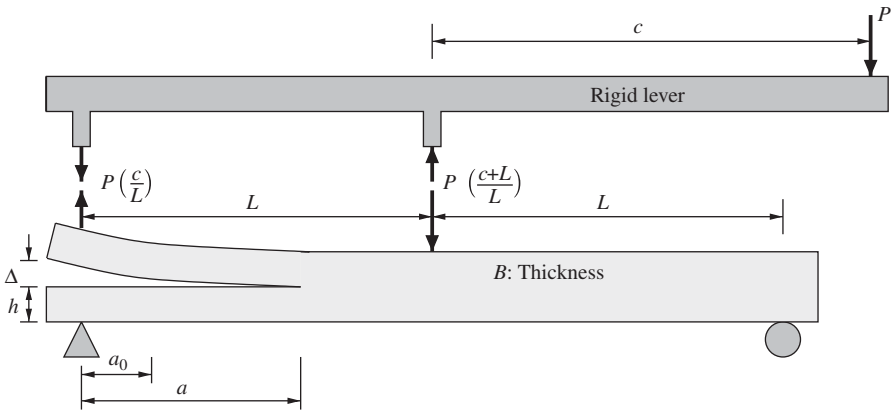


**Fig. 14.** Mixed mode bending test.

**Table 4**
Geometry of the MMB test specimen

| $L$ (mm) | $h$ (mm) | $a_0$ (mm) | $c$ (mm) | $B$ (mm) |
|---|---|---|---|---|
| 51 | 1.56 | 33.7 | 60 | 25.4 |

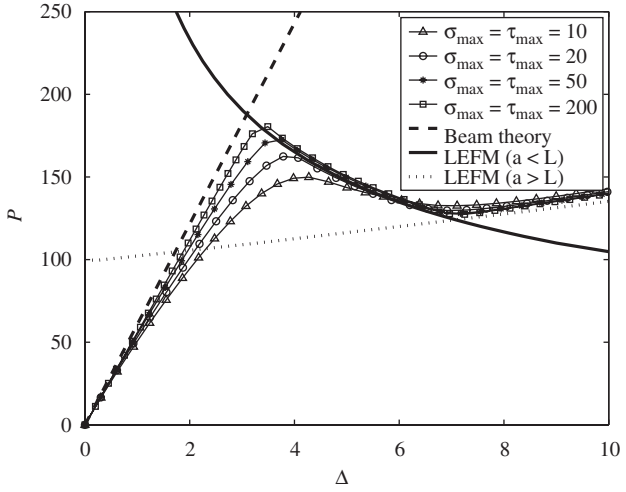


**Fig. 15.** Comparison between the analytical solutions and the numerical simulation results considering the same fracture energy ($\phi_n = \phi_t = 1\,N/m$).

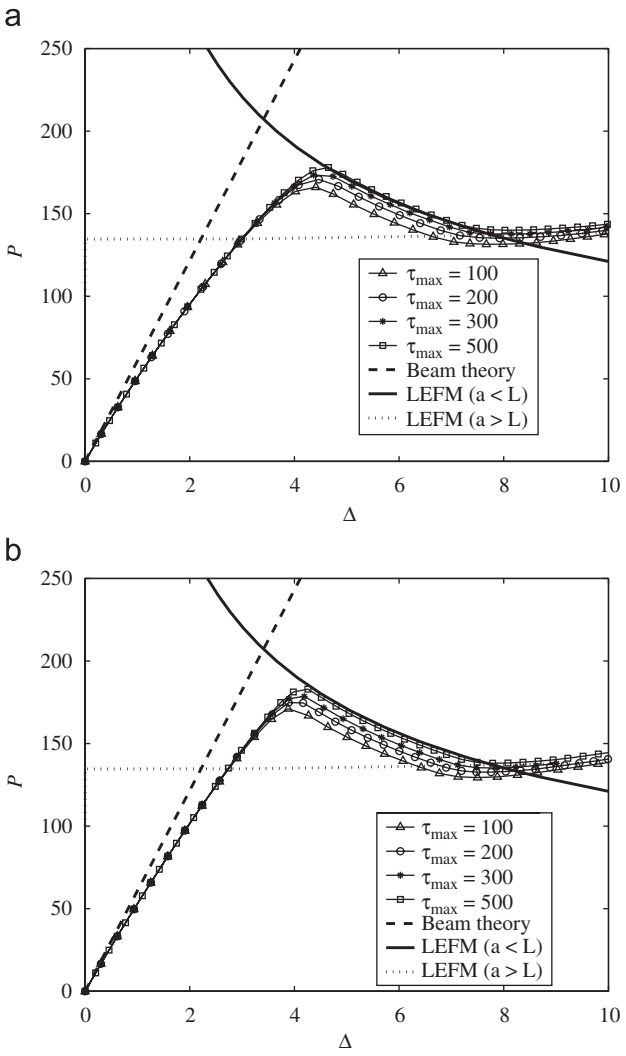


**Fig. 16.** Comparison between the analytical solutions and the numerical simulation results considering different fracture energies ($\phi_n = 1\,N/m$, $\phi_t = 2\,N/m$): (a) $\sigma_{max} = 10\,MPa$ and (b) $\sigma_{max} = 20\,MPa$.

122 GPa, and Poisson's ratio is 0.25. The shape parameters are fixed to be equal to three ($\alpha = \beta = 3$), while the initial slope indicators are selected as a small value within numerical stability limits, e.g. $(\lambda_n, \lambda_t) \in [0.005,\ 0.025]$. The specimen size is provided in Table 4. The numerical results are compared to the analytical solution provided by Mi et al. (1998). The analytical solution is given in Appendix A.

Fig. 15 compares the analytical solutions to the numerical results for the same fracture energy. The numerical simulation results converge to the analytical solutions with respect to the increase in the material cohesive strength. This is because the higher cohesive strength decreases the fracture process zone, and result in a more brittle failure.

Next, Fig. 16 illustrates the agreement of the analytical solutions and the numerical simulation results for the different fracture energies in modes I and II. Mode I fracture energy is 1 N/m and the mode II fracture energy increased to 2 N/m. Due to the increase of the mode II fracture energy, the analytical solution of linear elastic fracture mechanics (LEFM) shifts upward (with respect to Fig. 15) which represents a higher structural load capacity locally. In the simulations, the shear strength is increased from 100 to 500 MPa with a fixed normal strength of 10 MPa (Fig. 16(a)) and 20 MPa (Fig. 16(b)). The increase of the normal and shear strength demonstrates the convergence to the analytical solutions of the beam theory and the LEFM.

## 5. Conclusions

The unified potential-based constitutive model (PPR) is proposed for cohesive fracture to characterize different fracture energies ($\phi_n$,$\phi_t$) and cohesive strengths ($\sigma_{max}$, $\tau_{max}$). The potential-based model is applicable to various material softening responses, i.e. plateau-type (e.g. ductile), brittle and quasi-brittle, due to controllable softening given by the shape parameters ($\alpha$, $\beta$). The PPR model also includes initial slope indicators ($\lambda_n$, $\lambda_t$) to control elastic behavior, which can be selected as small values within numerical stability limits. The zero limit of the initial slope indicators leads to the potential function for extrinsic cohesive zone models. The cohesive interactions ($T_n$, $T_t$) are defined in a rectangular region associated with the final crack opening widths ($\delta_n$, $\delta_t$) and the conjugate final crack opening widths ($\bar{\delta}_n$, $\bar{\delta}_t$). The PPR potential-based model demonstrates that the work-of-separation depends on the separation paths, i.e. proportional and non-proportional paths, and monotonically changes from the mode I fracture energy to the mode II fracture energy with respect to the separation paths. The monotonic change of the work-of-separation demonstrates the consistency of the cohesive constitutive model. The numerical investigation of the mixed-mode bending test not only verifies the effect of different fracture energies (in modes I and II), but also demonstrates the convergence to the corresponding analytical solutions of beam theory and LEFM.

## Acknowledgments

We acknowledge support from the National Science Foundation (NSF) through Grant CMMI #0800805. The information presented in this paper is the sole opinion of the authors and does not necessarily reflect the views of the sponsoring agency.

## Appendix A. Analytical solution for the mixed-mode bending (MMB) test

The analytical solution for the mixed-mode bending (MMB) test is given by Mi et al. (1998). The solution consists of three parts based on the linear elastic beam theory (one part) and linear elastic fracture mechanics (two parts). The beam theory provides the linear analytical solution,

$$\Delta = \frac{2}{3}\left(\frac{3c-L}{4L}\right)\frac{Pa_0^3}{EI}, \tag{34}$$

where $I$ is the second moment of area and $E$ is the elastic modulus. Next, the concept of the fracture energy based on linear elastic fracture mechanics provides the following load ($P$) versus displacement relationship ($\Delta$),

$$\Delta = \frac{2P_I}{3EI}\left(\frac{8BEI}{8P_I^2/\phi_n + 3P_{II}^2/(8\phi_t)}\right)^{3/2}, \tag{35}$$

where

$$P_I = (3c-L)P/(4L), \quad P_{II} = (c+L)P/L. \tag{36}$$

This expression is valid when a crack length ($a$) is smaller than the half length ($L$) of a beam ($a<L$). When $a$ is greater than $L$, one obtains another expression,

$$\Delta = \frac{2}{3}\left(\frac{3c-L}{4L}\right)\frac{Pa^3}{EI}, \tag{37}$$

for the relationship between load ($P$) and displacement ($\Delta$). For a given load and displacement, the $a$ can be evaluated by solving following expression:

$$\left(\frac{8P_I^2}{\phi_n}+\frac{3P_{II}^2}{8\phi_t}-\frac{8P_IP_{II}}{\phi_t}\right)a^2-\left(\frac{3P_{II}^2L}{2\phi_t}-\frac{8P_IP_{II}L}{\phi_t}\right)a+\frac{3P_{II}^2L^2}{2\phi_t}-8BEI=0. \tag{38}$$

## References


Alfano, G., 2006. On the influence of the shape of the interface law on the application of cohesive-zone models. Compos. Sci. Technol. 66(6), 723–730 URL: http://dx.doi.org/10.1016/j.compscitech.2004.12.024.

Anderson, T.L., 1995. Fracture Mechanics: Fundamentals and Applications. CRC Press, Boca Raton.

ASTM, 2006. Standard test method for mixed mode I–mode II interlaminar fracture toughness of unidirectional fiber reinforced polymer matrix composites. Technical Report ASTM D 6671/D 6671M, ASTM International.

Banks-Sills, L., Bortman, Y., 1986. A mixed-mode fracture specimen: analysis and testing. Int. J. Fract. 30 (3), 181–201 URL: http://dx.doi.org/10.1007/BF00019776.

Barenblatt, G.I., 1959. The formation of equilibrium cracks during brittle fracture: general ideas and hypotheses, axially symmetric cracks. Appl. Math. Mech. 23 (3), 622–636.

Beltz, G.E., Rice, J.R., 1991. Dislocation nucleation versus cleavage decohesion at crack tips. In: Lowe, T.C., Rollett, A.D., Follansbee, P.S., Daehn, G.S. (Eds.), Modeling the Deformation of Crystalline Solids Presented. The Minerals, Metals & Materials Society (TMS), Havard University, Cambridge, MA, USA, pp. 457–480.

Benzeggagh, M.L., Kenane, M., 1996. Measurement of mixed-mode delamination fracture toughness of unidirectional glass/epoxy composites with mixed-mode bending apparatus. Compos. Sci. Technol. 56 (4), 439–449 URL: http://dx.doi.org/10.1016/0266-3538(96)00005-X.

Camacho, G.T., Ortiz, M., 1996. Computational modelling of impact damage in brittle materials. Int. J. Solids Struct. 33 (20–22), 2899–2938 URL: http://dx.doi.org/10.1016/0020-7683(95)00255-3.

Carpinteri, A., Ferrara, G., Melchiorri, G., 1989. Single edge notched specimen subjected to four point shear. An experimental investigation. In: Shah, S.P., Swartz, S.E., Barr, B. (Eds.), International Conference on Recent Developments in the Fracture of Concrete and Rock, September 20–22, 1990. Elsevier Applied Science, pp. 605–614.

Dugdale, D.S., 1960. Yielding of steel sheets containing slits. J. Mech. Phys. Solids 8 (2), 100–104.

Gao, H., Ji, B., 2003. Modeling fracture in nanomaterials via a virtual internal bond method. Eng. Fract. Mech. 70 (14), 1777–1791 URL: http://dx.doi.org/10.1016/S0013-7944(03)00124-3.

Gao, H., Klein, P., 1998. Numerical simulation of crack growth in an isotropic solid with randomized internal cohesive bonds. J. Mech. Phys. Solids 46 (2), 187–218 URL: http://dx.doi.org/10.1016/S0022-5096(97)00047-1.

Girifalco, L.A., Weizer, V.G., 1959. Application of the Morse potential function to cubic metals. Phys. Rev. 114 (3), 687–690.

Klein, P., Gao, H., 1998. Crack nucleation and growth as strain localization in a virtual-bond continuum. Eng. Fract. Mech. 61 (1), 21–48 URL: http://dx.doi.org/10.1016/S0013-7944(98)00048-4.

Mi, Y., Crisfield, M.A., Davies, G.A.O., Hellweg, H.B., 1998. Progressive delamination using interface elements. J. Compos. Mater. 32 (14), 1246–1272.

Moes, N., Belytschko, T., 2002. Extended finite element method for cohesive crack growth. Eng. Fract. Mech. 69 (7), 813–833 URL: http://dx.doi.org/10.1016/S0013-7944(01)00128-X.

Mooney, M., 1940. Theory of large elastic deformation. J. Appl. Phys. 11 (9), 582–592.

Needleman, A., 1987. A continuum model for void nucleation by inclusion debonding. J. Appl. Mech. Trans. ASME 54 (3), 525–531.

Needleman, A., 1990. An analysis of tensile decohesion along an interface. J. Mech. Phys. Solids 38 (3), 289–324 URL: http://dx.doi.org/10.1016/0022-5096(90)90001-K.

Ortiz, M., Pandolfi, A., 1999. Finite-deformation irreversible cohesive elements for three-dimensional crack-propagation analysis. Int. J. Numer. Methods Eng. 44 (9), 1267–1282 URL: http://dx.doi.org/10.1002/(SICI)1097-0207(19990330)44:9⟨1267::AID-NME486⟩3.3.CO;2-Z.

Park, K., Paulino, G.H., Roesler, J.R., 2008a. Potential-based cohesive constitutive model of mixed-mode fracture. In: Inaugural International Conference of the Engineering Mechanics Institute (EM 08). Minneapolis, MN.

Park, K., Paulino, G.H., Roesler, J.R., 2008b. Virtual internal pair-bond (VIPB) model for quasi-brittle materials. J. Eng. Mech. ASCE 134 (10), 856–866 URL: http://dx.doi.org/10.1061/(ASCE)0733-9399(2008)134:10(856).

Paulino, G.H., Park, K., Roesler, J.R., 2007. A novel potential-based approach for mixed-mode cohesive fracture simulation. In: Ninth US National Congress on Computational Mechanics (USNCCM 2007), San Francisco, CA.

Paulino, G.H., Park, K., Roesler, J.R., 2008. A unified potential-based cohesive model of mixed-mode fracture. In: Sixth International Conference on Computation of Shell and Spatial Structures (IASS-IACM 2008), Ithaca, NY.

Reeder, J.R., Crews Jr., J.H., 1990. Mixed-mode bending method for delamination testing. AIAA J. 28 (7), 1270–1276.

Remmers, J.J.C., de Borst, R., Needleman, A., 2008. The simulation of dynamic crack propagation using the cohesive segments method. J. Mech. Phys. Solids 56 (1), 70–92 URL: http://dx.doi.org/10.1016/j.jmps.2007.08.003.

Rice, J.R., 1992. Dislocation nucleation from a crack tip. an analysis based on the peierls concept. J. Mech. Phys. Solids 40 (2), 239–271.

Rose, J.H., Ferrante, J., Smith, J.R., 1981. Universal binding energy curves for metals and bimetallic interfaces. Phys. Rev. Lett. 47 (9), 675–678 URL: http://dx.doi.org/10.1103/PhysRevLett.47.675.

Shim, D.-J., Paulino, G.H., Dodds Jr., R.H., 2006. *J* resistance behavior in functionally graded materials using cohesive zone and modified boundary layer models. Int. J. Fract. 139 (1), 91–117 URL: http://dx.doi.org/10.1007/s10704-006-0024-4.

Song, S.H., Paulino, G.H., Buttlar, W.G., 2008. Influence of the cohesive zone model shape parameter on asphalt concrete fracture behavior. In: Paulino, G.H., Pindera, M.-J., Dodds Jr., R.H., Rochinha, F.A., Dave, E., Chen, L. (Eds.), Multiscale and Functionally Graded Material 2006 (M&FGM 2006). AIP Conference Proceedings, pp. 730–735. URL: http://link.aip.org/link/?APC/973/730/1.

Tadmor, E.B., Ortiz, M., Phillips, R., 1996. Quasicontinuum analysis of defects in solids. Philos. Mag. A 73 (6), 1529–1563.

Thiagarajan, G., Hsia, K.J., Huang, Y., 2004. Finite element implementation of virtual internal bond model for simulating crack behavior. Eng. Fract. Mech. 71 (3), 401–423 URL: http://dx.doi.org/10.1016/S0013-7944(03)00102-4.

Tvergaard, V., Hutchinson, J.W., 1992. The relation between crack growth resistance and fracture process parameters in elastic–plastic solids. J. Mech. Phy. Solids 40 (6), 1377–1397 URL: http://dx.doi.org/10.1016/0022-5096(92)90020-3.

Tvergaard, V., Hutchinson, J.W., 1993. The influence of plasticity on mixed mode interface toughness. J. Mech. Phys. Solids 41 (6), 1119–1135 URL: http://dx.doi.org/10.1016/0022-5096(93)90057-M.

van den Bosch, M., Schreurs, P.J.G., Geers, M.G.D., 2006. An improved description of the exponential Xu and Needleman cohesive zone law for mixed-mode decohesion. Eng. Fract. Mech. 73 (9), 1220–1234 URL: http://dx.doi.org/10.1016/j.engfracmech.2005.12.006.

Volokh, K.Y., 2004. Comparison between cohesive zone models. Commun. Numer. Methods Eng. 20 (11), 845–856 URL: http://dx.doi.org/10.1002/cnm.717.

Volokh, K.Y., Gao, H., 2005. On the modified virtual internal bond method. J. Appl. Mech. Trans. ASME 72 (6), 969–971 URL: http://dx.doi.org/10.1115/1.2047628.

Wells, G.N., Sluys, L.J., 2001. A new method for modelling cohesive cracks using finite elements. Int. J. Numer. Methods Eng. 50 (12), 2667–2682 URL: http://dx.doi.org/10.1002/nme.143.
Xu, X.P., Needleman, A., 1993. Void nucleation by inclusion debonding in a crystal matrix. Modelling Simulation Mater. Sci. Eng. 1 (2), 111–132 URL: http://dx.doi.org/10.1088/0965-0393/1/2/001.
Xu, X.P., Needleman, A., 1994. Numerical simulations of fast crack growth in brittle solids. J. Mech. Phys. Solids 42 (9), 1397–1434.
Yang, Q.D., Thouless, M.D., 2001. Mixed-mode fracture analyses of plastically-deforming adhesive joints. Int. J. Fract. 110 (2), 175–187 URL: http://dx.doi.org/10.1023/A:1010869706996.
Zhang, Z., Paulino, G.H., 2005. Cohesive zone modeling of dynamic failure in homogeneous and functionally graded materials. Int. J. Plasticity 21 (6), 1195–1254.
Zhang, Z., Paulino, G.H., Celes, W., 2007. Extrinsic cohesive modelling of dynamic fracture and microbranching instability in brittle materials. Int. J. Numer. Methods Eng. 72 (8), 893–923.
Zhou, F., Molinari, J.-F., Ramesh, K.T., 2005. A cohesive model based fragmentation analysis: effects of strain rate and initial defects distribution. Int. J. Solids Struct. 42 (18–19), 5181–5207 URL: http://dx.doi.org/10.1016/j.ijsolstr.2005.02.009.